Balloon regime: Drop elasticity leads to complete rebound

Diego Díaz,[1,*,†] Arivazhagan G. Balasubramanian,[1,2,*] Kasra Amini,[1] Xiaomei Li,[3] Fredrik Lundell,[1] Shervin Bagheri,[1,‡] and Outi Tammisola[1,2,§]

[1]*FLOW, Department of Engineering Mechanics, KTH Royal Institute of Technology, 100 44 Stockholm, Sweden*

[2]*Swedish e-Science Research Centre (SeRC), Stockholm, Sweden*

[3]*Institute for Chemical and Bioengineering, Department of Chemistry and Applied Bioscience, ETH Zürich, Zürich 8093, Switzerland*

(Received 19 January 2025; revised 16 September 2025; accepted 6 March 2026; published 7 April 2026)

When a highly elastic drop of a polymer solution hits a superhydrophobic surface at a high speed, a growing tail-like filament emerges vertically from the impact spot as the contact line recedes. Notably, the ligament transitions into a balloonlike shape before detaching completely from the surface (balloon regime). The ligament formation is attributed to liquid impalement upon impact into the surface protrusion spacing, and elastic forces due to polymers prevent ligament breakup. The detachment of the ligament happens when polymeric stresses balance or overcome the adhesion at the surface. This study shows that tuning droplet rheology and surface roughness enables droplets to rebound completely and without splashing at high impact speeds.

DOI: 10.1103/9gxn-thst

I. INTRODUCTION

Drop impact dynamics has fascinated researchers and engineers for over a century due to its fundamental significance in nature [1–3] and wide-ranging applications such as surface printing methods [4,5], energy harvesting [6], heat transfer [7], and so on [8,9]. Although the phenomenon is critical in many industrial processes, it can often lead to undesired effects such as splashing [8] and surface damage [10–12]. In particular, drop impact on superhydrophobic surfaces has garnered significant attention due to its potential for complete droplet rebound—a key feature for self-cleaning [13], anti-icing [14], and drag reduction purposes [15]. While the dynamics of Newtonian drops in these scenarios is relatively well understood, the behavior of non-Newtonian viscoelastic drops, especially at high impact speeds, remains poorly explored. This gap in understanding also limits our ability to design surfaces that can effectively repel complex liquids under high impact forces while mitigating surface damage.

Viscoelasticity, imparted by the addition of polymers to water, introduces unique features during drop impact, such as the formation of elongated threads that interact with surface microstructures [16,17]. These interactions challenge the conventional nonwetting behavior of superhydrophobic surfaces and raise fundamental questions about how elasticity and shear thinning influence droplet dynamics [18,19]. Importantly, achieving simultaneous droplet rebound and suppression of breakup and splashing at very high impact speeds has proven elusive [17,20–22].

In this article, we show that polymer additives can restore droplet rebound on superhydrophobic surfaces at very high impact speeds, a feat previously not observed for non-Newtonian drops. Through experiments and numerical simulations, we discover a regime—termed the balloon regime—characterized by the formation and complete detachment of a vertical ligament during droplet rebound. This ligament rebound is governed by the interplay of liquid penetration into surface microstructures and elastic forces in the ligament (in addition to gravity and inertia of the main droplet). Our findings introduce an approach for controlling droplet dynamics by leveraging the rheology of polymer-infused liquids and tailored preparation of surface microstructures. This provides a pathway to design conditions that retain liquid-repellent properties at high impact speeds, without leaving satellite drops. Here, we will outline the key physical factors responsible for *balloon regime* by experiments, theory, and numerical analysis.

II. EXPERIMENTAL

Viscoelastic aqueous drops of initial diameter $D_0 = 2.5$ mm and impact speed v_0 ranging from 0.23 to 3.4 m/s were dispensed using a stainless-steel needle attached to a syringe pump onto a superhydrophobic surface. The surface was prepared by spray coating three times glass slides with silanized silica nanoparticles (Glaco Soft99) after plasma activation (see Secs. I A and I B of the Supplemental Material [23] for details on surface preparation and experimental setup). The viscoelastic liquid solution was prepared by mixing polyacrylamide (PAM, Mw $> 15 \times 10^6$ Da) in deionized water

*These authors contributed equally to this work.
†Contact author: didd@kth.se
‡Contact author: shervinb@kth.se
§Contact author: outi@mech.kth.se

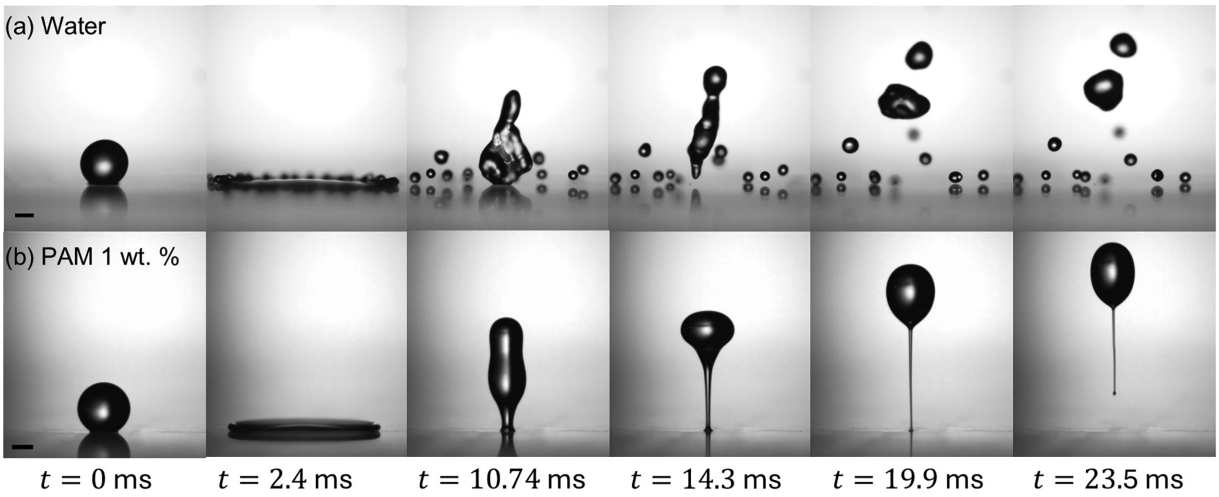

FIG. 1. (a) Time-lapsed snapshots of a water drop and (b) PAM 1 wt% drop impacting the superhydrophobic surface at We = 204. Scale bars represent 1 mm.

in concentrations C_w (by mass) between 0.025 and 1 wt%. Rheometric measurements evidenced shear thinning for all solutions, with zero shear-rate viscosities ranging from 7 to 25×10^3 mPa s (see Sec. I C of the Supplemental Material [23] for rheological characterization of liquids used in this study). The impact process was recorded simultaneously from the side and bottom views by two high-speed cameras at up to 4900 fps. All PAM concentrations practically showed the same static contact angles as water ($\Theta_s \sim 167^\circ \pm 2^\circ$).

III. BALLOON REGIME

The Weber number $\mathrm{We} = \rho v_0^2 D_0/\sigma$ represents the ratio of drop inertia to surface tension ($2 < \mathrm{We} < 408$), where ρ is fluid density and σ denotes the surface tension coefficient. Here, we use the density and surface tension of water for all solutions ($\rho = 1000$ kg/m^3 and $\sigma = 72$ mN/m), because PAM solutions up to 1% in the studied range are expected to show negligible changes in density, and pendant drop measurements indicate only a minor variation in surface tension. When $2 < \mathrm{We} < 136$, drops rebound completely for both water and viscoelastic liquids [Fig. S1(d) and Sec. I B of the Supplemental Material [23]]. Only for water, secondary drops are ejected from the top part of the primary drop. When We > 136, water drops exhibited splashing behavior [Fig. 1(a)], with complete surface detachment, but leaving numerous satellite drops behind. However, splashing is completely suppressed for viscoelastic drops ($C_w > 0.025\%$), which during the receding phase form a ligament that extends and becomes thinner over time, whereby a head droplet arises at the top [Fig. 1(b) and Fig. S3 and Supplemental Movie S1 in the Supplemental Material [23]]. The ligament formation becomes more prominent with increasing polymer concentrations. Eventually, the ligament as a whole detaches from the surface, resulting in a bottom tail that retracts back to the primary drop. We can remark on two important aspects of this phenomenon. First, a complete rebound is achieved for the entire range of We considered in this work, in contrast to previous studies where bouncing behavior was suppressed by increasing polymer concentrations. Second, right before bouncing, the head drop gives rise to a balloonlike shape for PAM at 0.5 and 1 wt%. Such behavior has not been reported before for impacting drops.

IV. SURFACE IMPALEMENT

The balloon regime of droplet impact starts with penetration into surface microstructures, leading to a transition from the Cassie-Baxter [24] to Wenzel [25] state. The superhydrophobic surface is formed by self-assembled silanized silica nanoparticles with a fractal-type structure. This allows the formation of air pockets, reducing the surface energy and increasing the repellency to water. When a drop hits a structured surface, the balance between the wetting and antiwetting pressure determines the wetting states [26,27]. Wetting pressure is dominated by water hammer pressure $P_H = \rho C v_0/5$ [28], with C the speed of sound in water (1497 m/s [29]), while the antiwetting pressure is the capillary pressure $P_C = -2\sqrt{2}\sigma \cos\theta_a/r$ [28,30], where θ_a is the advancing contact angle of the flat surface ($\approx 120^\circ$) and r is the spacing between the surface microstructures. Surface penetration happens when $P_H = P_C$, $r \approx 5\sigma/\rho C v_0$, which at We = 136 (where we start to observe ligament formation) is ≈ 0.1 μm. This is in good agreement with the surface topography produced by the Glaco coating [31]. Simulations (Fig. S14 and Sec. VII F of the Supplemental Material [23]) indicate that wetting pressure is highest directly at impact; hence, we postulate that impalement initiates locally at the moment of impact, creating a pinning/sticking point. As the liquid spreads outward, pressure decreases leading to less impalement [17,32]. As a result, pinninglike effect and ligament formation arise during the receding phase, where the contact line moves over the wetted area. Just before detachment, as the ligament reaches its minimum thickness, it pulls upward, overcoming the sticking point (full impalement). This behavior is supported by bottom-view impact images, which reveal a central region of complete impalement encircled by a concentric zone of less impalement [Fig. S4(b) and Sec. III of the Supplemental Material [23]]. The area of this region tends to increase in area with We, suggesting a wider impalement.

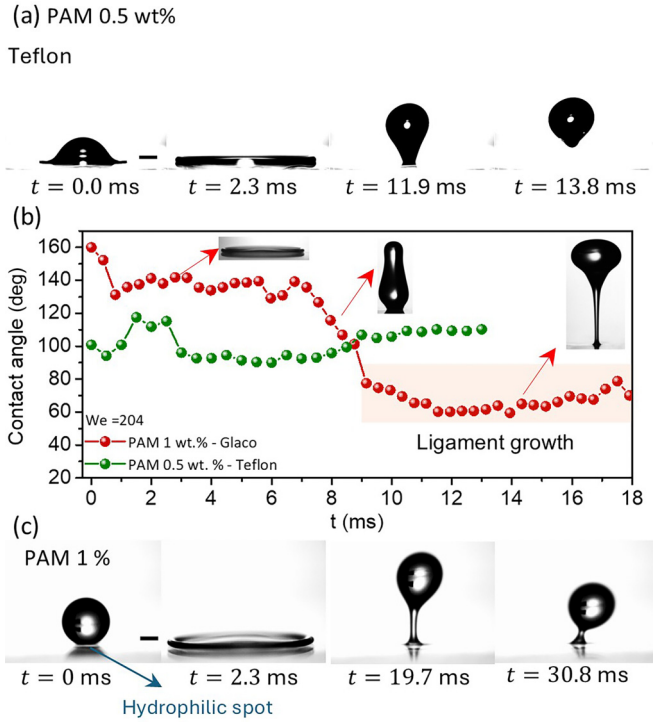

FIG. 2. (a) PAM 0.5 wt% droplet impacting a hydrophobic Teflon surface at We = 204. (b) Dynamic contact angle over time for the case shown in panel (a) (green dots, rebound without ligaments) and in Fig. 1(b) (red dots, rebound with ligaments). (c) PAM 1 wt% droplet impacting on the superhydrophobic surface with a hydrophilic spot at We = 204. Scale bar represents 1 mm.

V. LIGAMENT FORMATION

Two key conditions for ligament formation are (1) liquid impalement with Cassie-Wenzel transition during spreading phase and (2) contact line pining due to liquid impalement during receding phase. To validate condition (1), we performed droplet impact experiments on a smooth hydrophobic Teflon AF film layer (∼60 nm, $\Theta_s = 120^\circ \pm 2^\circ$) on a sputter-coated glass slide. Preparation methods were in accordance to that outlined in the study by Li *et al.* [33]. The lower roughness of Teflon ($R_q \sim 5$ nm) ensures the absence of microstructures with air pockets. As a result, liquid impalement is improbable, which allows the droplet to remain in the Wenzel state during the whole impact process. To isolate the role of substrate texture, we compared PAM concentrations and We values where ligaments were observed. Notably, ligament formation was completely suppressed by the smooth Teflon surface [Fig. 2(a) and Fig. S5 and Sec. IV of the Supplemental Material [23]]. On the superhydrophobic surface, the dynamic contact angle (measured by fitting method from Shumaly *et al.* [34]) remains at ∼140° during spreading ($t \lessapprox 2$ ms) and part of receding (2 ms $< t <$ 8 ms) phase. Afterward, the dynamic contact angle further decreases when a ligament starts to form ($t \approx 8$ ms) and finally reaches a receding contact angle plateau $\theta_r \sim 60^\circ$ [Fig. 2(b), red markers]. In contrast, on smooth Teflon surface, the contact angle during the drop recoil is nearly constant [Fig. 2(b), green markers] indicates that droplet remains in the Wenzel state without liquid impalement. Thus, the Cassie-Wenzel transition is a necessary condition for supporting ligament formation through an abrupt decrease in θ_r.

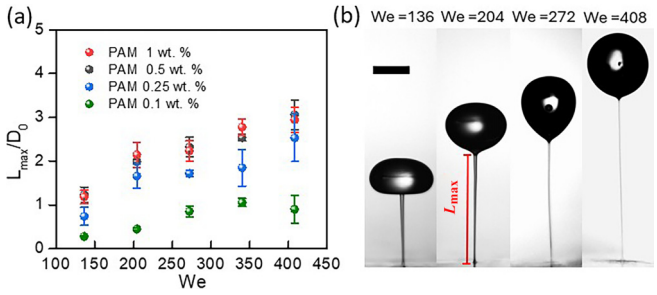

FIG. 3. (a) Maximum ligament length $L_{\max}$ scaled by the drop diameter D_0 as a function of We. (b) Snapshots of $L_{\max}$ at different We. Scale bar represents 2.5 mm.

To validate condition (2), we prepared the same superhydrophobic surface with a hydrophilic spot of 0.8 mm diameter. To prepare the sample, we covered the glass slide by a chrome vanadium steel material of 0.8 mm diameter before spraying the surface with silica nanoparticles. Subsequently, we dispensed PAM drops on this surface with the same conditions as the case in Fig. 1(b). The experiment revealed the formation of a shorter ligament pinned to the spot that grows without detachment as depicted in Fig. 2(c). Therefore, contact line pinning is also one of the key conditions to generate ligaments.

VI. LIGAMENT GROWTH

To elucidate the dominant forces, the maximum ligament length $L_{\max}$ reached just prior to detachment was measured for all different concentrations. Figures 3(a) and 3(b) indicate that the normalized maximum ligament length, $L_{\max}/D_0$, is directly proportional to fluid inertia ($L_{\max} \propto$ We) and also increases with polymer concentration. As discussed earlier, higher We enlarge the impalement area. This prolongs the detachment time, thereby the leading droplet continues to ascend, promoting further elongation of the ligament.

The height of the droplet centroid in time $Y_c(t)$ for the full detachment scenario [Fig. 4(a)] is well described by a ballistic model $Y_c(t) = Y_{c_0} + v_{y0}t - \frac{1}{2}gt^2$, where Y_{c_0} is the initial vertical position of Y_c when a ligament starts to form (neck emerging below), v_{y0} the vertical speed at the moment of ligament formation (dY_c/dt), and g the acceleration of gravity. This suggests that the position of the droplet centroid is given by a balance of gravity and inertia. The integrated difference in potential energy ΔE_p up to the maximum height between the model and the experiments provides a maximum estimate on the total energy dissipated by viscous and elastic forces. In this way, the total dissipative force $\Delta E_p/L_{\max} \sim 10^{-6}$ N is at least one order of magnitude smaller than the gravitational force $\rho V g \sim 8.5 \times 10^{-5}$ N (here, V is the drop volume). In the case of surface with hydrophilic spot, Y_c is up to four times lower than the complete rebound scenario. The ballistic model fails to fully capture the main drop motion and overestimates $L_{\max}$ (Fig. S7 and Sec. V of the Supplemental Material [23]).

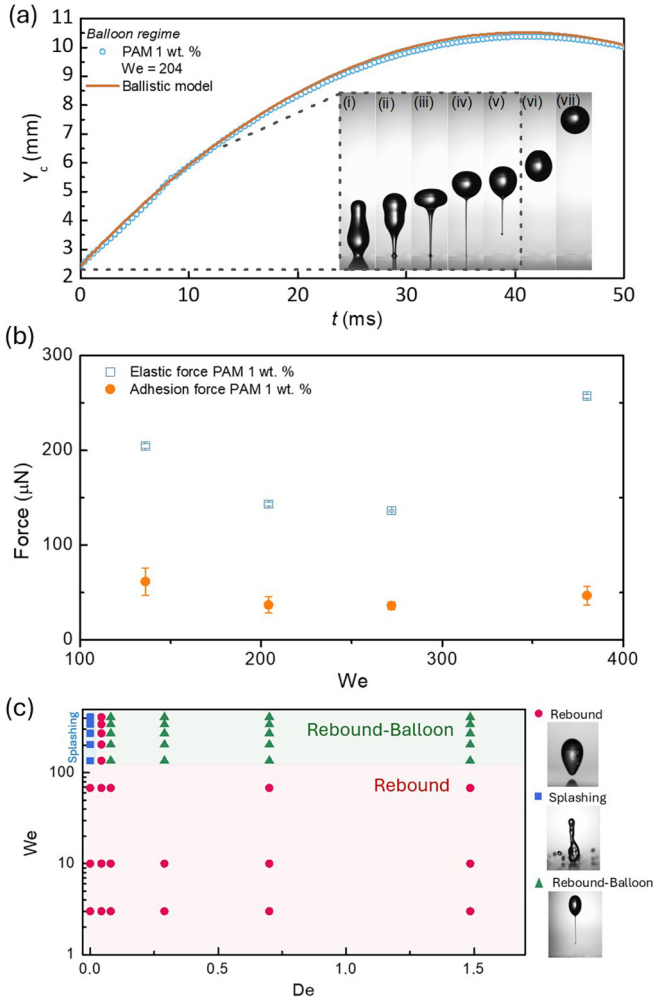

FIG. 4. (a) Height of the droplet centroid in time for PAM 1 wt%. Insets (i)–(vii) represent the time lapses of the ligament growth: $t = 3$, 7, 9, 13, 14, 19, and 43 ms, respectively. (b) Elastic and adhesion forces for PAM 1 wt% at different Weber numbers. (c) Phase diagram depicting the different droplet behavior based on the impact velocity (We) and elastic stress relaxation timescale of the liquid (De).

This discrepancy arises from the higher adhesion to the bare glass surface than to the nanoparticles of the Glaco coating.

Concluding, in the drop impact cases of viscoelastic liquid on a superhydrophobic surface, the ligament length is determined mainly by the rebound velocity and gravitational forces. Although the elastic stresses are not dominant in determining the ligament length, they are crucial in sustaining the ligament from possible breakup and detachment from surface. The conditions observed locally at the ligament resemble those in the capillary breakup extensional rheometry [35–37], with the minimum radius of the ligament decaying exponentially with time (Fig. S8 and Sec. VI of the Supplemental Material [23]).

VII. DETACHMENT FROM SURFACE

During ligament growth phase, axial elastic stresses $\tau_{p,zz}$ develop along the filament. Our hypothesis is that these elastic stresses must balance or exceed adhesion forces at the contact line, enabling the complete detachment of the ligament, leading to a full rebound of the droplet. To test the validity of this hypothesis, we estimate and compare the axial elastic force $F_e = \tau_{p,zz}\pi R_{\min}^2$ within the ligament to the corresponding adhesion force at the wall, $F_a = 2\pi R_w \sigma(1 + \cos(\theta_r))$, where $R_{\min}$ is the minimum ligament thickness, R_w is the wetted radius, and θ_r is the receding contact angle. The adhesion force at the substrate was estimated based on the Young-Dupré equation [38].

We consider two representative cases for PAM 1 wt %: (1) We = 272 on the superhydrophobic surface with full ligament detachment and (2) We = 204 in the presence of a hydrophilic spot where ligament does not detach. In the detaching case, we estimated $F_a \in \mathcal{O}(10)$ μN and $F_e \in \mathcal{O}(100)$ μN. This substantial difference suggests that elastic stresses actively aid in overcoming adhesion and promote ligament detachment (see Secs. VII and VIII of the Supplemental Material [23] for details on the estimation of axial elastic stress), which can also be observed at different We where complete rebound occurs [Fig. 4(b)], and when $R_{\min}$ and R_w are within our limit resolution (20 μm). Values of R_w and $R_{\min}$ range between 100 and 80 μm and 60 and 27 μm, respectively. Note that elastic stresses are calculated at R_w; therefore, the tensile elastic forces along the ligament height are not necessarily uniform due to local deformations of the liquid material. Elastic forces may therefore be smaller at the anchored base. Moreover, the impaled area contributes additional adhesion at the base. This likely overestimates F_e and underestimates F_{adh}, so immediate detachment can be reasonably reached when $F_e \sim F_{\text{adh}}$, with the general condition $F_e \gtrsim F_{\text{adh}}$. In contrast, for the hydrophilic spot case, the adhesion force increases significantly to approximately $\mathcal{O}(100)$ μN, while $F_e \in \mathcal{O}(10)$ μN. Since the elastic stress is insufficient to decisively overcome adhesion, the detachment of ligament is inhibited.

To further confirm that the detachment is due to elastic forces but not due to higher viscosity of the polymeric droplets, we repeated the experiments with water-glycerol droplets that are viscous but not elastic. Water drops containing 50% glycerol (viscosity $\eta = 7$ mPa s) and impacting on Glaco-coated surfaces consistently exhibited contact line pinning and droplet elongation, but only partial rebound with a satellite droplet remaining on the surface (see Sec. IX of the Supplemental Material [23]).

These findings reinforce the crucial interplay between interfacial adhesion and elastic stresses in governing detachment dynamics. The ligament retraction velocity is observed to increase with axial elastic stress. This retraction speed can be estimated by $\sqrt{(\sigma/\rho R_{\min}) + (\tau_{p,zz}/\rho)}$ [39], where the second term reflects the contribution of elastic stress. In agreement with this, we observe higher retraction velocities at the moment of detachment for droplets with greater polymer concentration.

VIII. PHASE DIAGRAM

Finally, we summarize the observed regimes of droplet behavior on the Glaco-coated surface in a phase diagram [Fig. 4(c)], which delineates the transition between bouncing,

splashing, and ligament-detachment-based rebound (balloon regime) as a function of impact conditions and viscoelastic properties. Here, the impact conditions refer to the impact velocity, characterized by Weber number We. The elastic property of the fluid is based on Deborah number De (defined as $\mathrm{De} = \lambda_e/\sqrt{\rho D_0^3/\sigma}$, where λ_e corresponds to the extensional relaxation timescale of the liquid. We observe the balloon regime at large We and De. These results underscore the essential role of elastic stresses in enabling rebound via ligament detachment, offering a pathway for tunable control of viscoelastic drop dynamics on textured surfaces. This paves the way for the design and optimization of textured surfaces tailored for droplets of real-life complex fluids, or conversely, changing the impact outcome by tuning the rheology of the droplet.

IX. CONCLUSIONS

To conclude, we identify a previously unreported regime of viscoelastic droplet impact on superhydrophobic surfaces—termed the *balloon regime*—characterized by the formation of a slender ligament that grows and ultimately detaches completely, enabling rebound. We attribute the origin of this phenomenon to liquid impalement into surface microstructures, corresponding to a Cassie-to-Wenzel transition. This is supported by a pronounced decrease in the dynamic contact angle during the receding phase. The high elasticity of the liquid enables the stable elongation of the ligament from the impact site and facilitates its complete detachment from the substrate. Analysis of the droplet's centroid trajectory reveals that ligament growth in time is primarily governed by the rebound velocity and gravitational forces. Furthermore, we demonstrate that ligament formation is highly sensitive to surface roughness and wettability, offering a means of control. These findings offer insights for applications involving viscoelastic drop deposition, where controlling instabilities is essential—for instance, in the printing of non-Newtonian fluids, agricultural spraying, and other industrial processes involving complex fluids.

ACKNOWLEDGMENTS

The authors acknowledge financial support from the European Union through the European Research Council (ERC) Grant No. "2019-StG-852529, MUCUS" and the European Union's Horizon 2020 research and innovation program under the Marie Skłodowska-Curie Grant Agreement No. 955605 YIELDGAP. S.B. gratefully acknowledges support from the ERC project (CoG-101088639 LUBFLOW). We thank Professor David Quéré for the insightful discussions.

DATA AVAILABILITY

The data supporting this study's findings are available within the article.

[1] Y. S. Joung and C. R. Buie, Aerosol generation by raindrop impact on soil, Nat. Commun. **6**, 6083 (2015).
[2] T. Gilet and L. Bourouiba, Fluid fragmentation shapes rain-induced foliar disease transmission, J. R. Soc. Interface **12**, 20141092 (2015).
[3] L. Bourouiba, The fluid dynamics of disease transmission, Annu. Rev. Fluid Mech. **53**, 473 (2021).
[4] C. D. Modak, A. Kumar, A. Tripathy, and P. Sen, Drop impact printing, Nat. Commun. **11**, 4327 (2020).
[5] D. Lohse, Fundamental fluid dynamics challenges in inkjet printing, Annu. Rev. Fluid Mech. **54**, 349 (2022).
[6] H. Wu, N. Mendel, D. van den Ende, G. Zhou, and F. Mugele, Energy harvesting from drops impacting onto charged surfaces, Phys. Rev. Lett. **125**, 078301 (2020).
[7] S. Shiri and J. C. Bird, Heat exchange between a bouncing drop and a superhydrophobic substrate, Proc. Natl. Acad. Sci. USA **114**, 6930 (2017).
[8] A. L. Yarin, Drop impact dynamics: Splashing, spreading, receding, bouncing …, Annu. Rev. Fluid Mech. **38**, 159 (2006).
[9] A. M. Karim, Physics of droplet impact on various substrates and its current advancements in interfacial science: A review, J. Appl. Phys. **133**, 030701 (2023).
[10] N. Fujisawa, T. Yamagata, K. Hayashi, and T. Takano, Experiments on liquid droplet impingement erosion by high-speed spray, Nucl. Eng. Des. **250**, 101 (2012).
[11] J. Poloprudský, A. Chlupová, I. Šulák, T. Kruml, and S. Hloch, Surface and subsurface analysis of stainless steel and titanium alloys exposed to ultrasonic pulsating water jet, Materials **14**, 5212 (2021).
[12] A. Nastic, M. Vijay, A. Tieu, and B. Jodoin, High speed water droplet impact erosive behavior on dry and wet pulsed waterjet treated surfaces, Phys. Fluids **35**, 053609 (2023).
[13] A. Milionis, C. S. Sharma, R. Hopf, M. Uggowitzer, I. S. Bayer, and D. Poulikakos, Engineering fully organic and biodegradable superhydrophobic materials, Adv. Mater. Interfaces **6**, 1801202 (2019).
[14] T. Zhu, Y. Cheng, J. Huang, J. Xiong, M. Ge, J. Mao, Z. Liu, X. Dong, Z. Chen, and Y. Lai, A transparent superhydrophobic coating with mechanochemical robustness for anti-icing, photocatalysis and self-cleaning, Chem. Eng. J. **399**, 125746 (2020).
[15] Y. Zhang, Z. Zhang, J. Yang, Y. Yue, and H. Zhang, A review of recent advances in superhydrophobic surfaces and their applications in drag reduction and heat transfer, Nanomaterials **12**, 44 (2021).
[16] H. Xu, A. Clarke, J. P. Rothstein, and R. J. Poole, Sliding viscoelastic drops on slippery surfaces, Appl. Phys. Lett. **108**, 241602 (2016).
[17] L. Chen, Y. Wang, X. Peng, Q. Zhu, and K. Zhang, Impact dynamics of aqueous polymer droplets on superhydrophobic surfaces, Macromolecules **51**, 7817 (2018).
[18] L.-H. Luu and Y. Forterre, Giant drag reduction in complex fluid drops on rough hydrophobic surfaces, Phys. Rev. Lett. **110**, 184501 (2013).
[19] R. Rabbi, A. Kiyama, J. S. Allen, and T. Truscott, Droplet lift-off from hydrophobic surfaces from impact with soft-hydrogel spheres, Commun. Phys. **5**, 331 (2022).

[20] V. Bergeron, D. Bonn, J. Y. Martin, and L. Vovelle, Controlling droplet deposition with polymer additives, Nature (London) **405**, 772 (2000).
[21] D. Bartolo, A. Boudaoud, G. Narcy, and D. Bonn, Dynamics of non-Newtonian droplets, Phys. Rev. Lett. **99**, 174502 (2007).
[22] P. Dhar, S. R. Mishra, and D. Samanta, Onset of rebound suppression in non-Newtonian droplets post-impact on superhydrophobic surfaces, Phys. Rev. Fluids **4**, 103303 (2019).
[23] See Supplemental Material at http://link.aps.org/supplemental/10.1103/9gxn-thst for a description of experimental, numerical methods, and Supplemental Movie S1, which includes Refs. [38–55].
[24] A. B. D. Cassie and S. Baxter, Wettability of porous surfaces, Trans. Faraday Soc. **40**, 546 (1944).
[25] R. N. Wenzel, Resistance of solid surfaces to wetting by water, Ind. Eng. Chem. **28**, 988 (1936).
[26] D. Bartolo, F. Bouamrirene, E. Verneuil, A. Buguin, P. Silberzan, and S. Moulinet, Bouncing or sticky droplets: Impalement transitions on superhydrophobic micropatterned surfaces, Europhys. Lett. **74**, 299 (2006).
[27] M. Reyssat, A. Pépin, F. Marty, Y. Chen, and D. Quéré, Bouncing transitions on microtextured materials, Europhys. Lett. **74**, 306 (2006).
[28] T. Deng, K. K. Varanasi, M. Hsu, N. Bhate, C. Keimel, J. Stein, and M. Blohm, Nonwetting of impinging droplets on textured surfaces, Appl. Phys. Lett. **94**, 133109 (2009).
[29] V. A. Del Grosso and C. W. Mader, Speed of sound in pure water, J. Acoust. Soc. Am. **52**, 1442 (1972).
[30] B. Zhao, X. Wang, K. Zhang, L. Chen, and X. Deng, Impact of viscous droplets on superamphiphobic surfaces, Langmuir **33**, 144 (2017).
[31] K. R. Langley, E. Q. Li, I. U. Vakarelski, and S. T. Thoroddsen, The air entrapment under a drop impacting on a nano-rough surface, Soft Matter **14**, 7586 (2018).
[32] X. Deng, F. Schellenberger, P. Papadopoulos, D. Vollmer, and H.-J. Butt, Liquid drops impacting superamphiphobic coatings, Langmuir **29**, 7847 (2013).
[33] X. Li, *et al.*, Spontaneous charging affects the motion of sliding drops, Nat. Phys. **18**, 713 (2022).
[34] S. Shumaly, F. Darvish, X. Li, A. Saal, C. Hinduja, W. Steffen, O. Kukharenko, H.-J. Butt, and R. Berger, Deep learning to analyze sliding drops, Langmuir **39**, 1111 (2023).
[35] A. V. Bazilevskii, V. M. Entov, M. M. Lerner, and A. N. Rozhkov, Failure of polymer solution filaments, Polym. Sci. Ser. A **39**, 316 (1997).
[36] S. L. Anna and G. H. McKinley, Elasto-capillary thinning and breakup of model elastic liquids, J. Rheol. **45**, 115 (2001).
[37] P. P. Bhat, S. Appathurai, M. T. Harris, M. Pasquali, G. H. McKinley, and O. A. Basaran, Formation of beads-on-a-string structures during break-up of viscoelastic filaments, Nat. Phys. **6**, 625 (2010).
[38] J. W. Drelich, L. Boinovich, E. Chibowski, C. Della Volpe, L. Hołysz, A. Marmur, and S. Siboni, Contact angles: History of over 200 years of open questions, Surf. Innov. **8**, 3 (2020).
[39] U. Sen, C. Datt, T. Segers, H. Wijshoff, J. H. Snoeijer, M. Versluis, and D. Lohse, The retraction of jetted slender viscoelastic liquid filaments, J. Fluid Mech. **929**, A25 (2021).
[40] G. Bradski, The OpenCV Library, Dr. Dobb's J. Softw. Tools **25**, 120 (2000).
[41] W. H. Press and S. A. Teukolsky, Savitzky–Golay smoothing filters, Comput. Phys. **4**, 669 (1990).
[42] J. Dinic, Y. Zhang, L. N. Jimenez, and V. Sharma, Extensional relaxation times of dilute, aqueous polymer solutions, ACS Macro Lett. **4**, 804 (2015).
[43] A. Franco-Gómez, H. Onuki, Y. Yokoyama, Y. Nagatsu, and Y. Tagawa, Effect of liquid elasticity on the behaviour of high-speed focused jets, Exp. Fluids **62**, 41 (2021).
[44] S. Popinet, An accurate adaptive solver for surface-tension-driven interfacial flows, J. Comput. Phys. **228**, 5838 (2009).
[45] S. Popinet *et al.*, Basilisk C (2013–2024), http://basilisk.fr (accessed 16 December 2024).
[46] S. Popinet, Numerical models of surface tension, Annu. Rev. Fluid Mech. **50**, 49 (2018).
[47] J. U. Brackbill, D. B. Kothe, and C. Zemach, A continuum method for modeling surface tension, J. Comput. Phys. **100**, 335 (1992).
[48] R. Comminal, J. Spangenberg, and J. H. Hattel, Robust simulations of viscoelastic flows at high Weissenberg numbers with the streamfunction/log-conformation formulation, J. Non-Newtonian Fluid Mech. **223**, 37 (2015).
[49] R. Fattal and R. Kupferman, Constitutive laws for the matrix-logarithm of the conformation tensor, J. Non-Newtonian Fluid Mech. **123**, 281 (2004).
[50] J. H. Snoeijer, A. Pandey, M. A. Herrada, and J. Eggers, The relationship between viscoelasticity and elasticity, Proc. R. Soc. A **476**, 20200419 (2020).
[51] B. Purnode and M. J. Crochet, Polymer solution characterization with the fene-p model, J. Non-Newtonian Fluid Mech. **77**, 1 (1998).
[52] P. C. Sousa, P. M. Coelho, M. S. N. Oliveira, and M. A. Alves, Polymer solution characterization with the fene-p model, Chem. Eng. Sci. **66**, 998 (2011).
[53] A. Dixit, A. Oratis, K. Zinelis, D. Lohse, and V. Sanjay, Viscoelastic Worthington jets and droplets produced by bursting bubbles, J. Fluid Mech. **1010**, A2 (2025).
[54] K. Yokoi, D. Vadillo, J. Hinch, and I. Hutchings, Numerical studies of the influence of the dynamic contact angle on a droplet impacting on a dry surface, Phys. Fluids **21**, 072102 (2009).
[55] L. Gordillo, T.-P. Sun, and X. Cheng, Dynamics of drop impact on solid surfaces: Evolution of impact force and self-similar spreading, J. Fluid Mech. **840**, 190 (2018).